Eng. Sci., 2025, **38**, 1844

Engineered Science
DOI: https://dx.doi.org/10.30919/es1844

Synergistic Sulfur Vacancy and Neodymium(Nd) Doping Enable Switchable Saturable Absorption/Reverse Saturable Absorption in Molybdenum Disulfide Nanosheets at Near-Infrared

Lihua Liu,[1] Zhixiang Cui,[1,#,*] Hengyu Zhao,[3] Jia Pan,[1] Sen Zeng,[1] Qianting Wang,[1,2] Xiaolong Wang[4] and Junhui Si[1,*]

Abstract

This study overcomes the near-infrared (NIR) limitation of MoS_2 through a synergistic strategy of incorporating sulfur vacancies (V_S) and neodymium (Nd^{3+}) doping. Hydrothermally synthesized Nd:MoS_2 nanosheets exhibit a drastically reduced optical bandgap from 1.28 eV to 0.45 eV, a doubling of photoluminescence (PL) intensity, and a newly acquired nonlinear optical (NLO) response at 1064 nm. This approach enables intensity-dependent switching between saturable absorption (SA) and reverse saturable absorption (RSA), while also enhancing the RSA effect at 532 nm. Femtosecond transient absorption spectroscopy and density functional theory (DFT) calculations reveal that the synergy between Nd^{3+} energy levels and VS defect states shortens the carrier trapping time (τ_1) to 1.2 ps and prolongs the non-radiative recombination lifetime (τ_2) to 84.8 ps. This process drives a shift in the NLO mechanism from ground-state to excited-state absorption, underpinning the novel NIR RSA effect. The work provides critical insights for designing advanced NIR photonic devices such as optical limiters and switches.

Keywords: Sulfur vacancy; Neodymium (Nd) doping; Nonlinear optical (NLO) materials; Molybdenum disulfide (MoS_2); SA-to-RSA switching.
Received: 03 September 2025; Revised: 20 October 2025; Accepted: 27 October 2025
Article type: Research article.

1. Introduction

The study of nonlinear optical (NLO) materials is one of the key factors driving the continuous development of optoelectronic technology. These materials have broad application prospects in fields such as pulse laser generation, optical limiting, multi-photon pumping lasers, and optoelectronic detection.[1] The NLO absorption effect, which refers to the property of a material's absorption coefficient changing with the incident light intensity, is the core physical mechanism for realizing the above-mentioned functionalities. Among various NLO materials, two-dimensional (2D) materials exhibit great application potential due to their unique electronic structures and optical properties.[2] Among them, 2D Transition Metal Dichalcogenides (TMDCs) materials (such as MoS_2) have attracted significant attention in nanoelectronics and optoelectronic devices due to their broadband tunable optical bandgap (E_g) ranging from several eV to sub-eV through modification. As a typical TMDCs material, the 2H phase of MoS_2 exhibits significantly better thermodynamic stability compared to the 1T and 3R phases, and has become a research focus.[3-5] Its intrinsic E_g ranges from 1.28 to 1.98 eV, enabling efficient absorption of the most energetic visible light portion (400-700 nm) in the solar spectrum. However, this intrinsic Eg severely limits its ability to absorb light in the near-infrared (NIR) region with wavelengths > 1000 nm.[6,7] In the NIR region (*e.g.*, 1064 nm, photon energy ~1.16 eV), the photon energy is lower than the E_g of the material and cannot effectively excite intrinsic electronic transitions, resulting in a significant decrease in single-photon response efficiency. This limitation hinders its application in NIR optoelectronic devices.[8] Therefore, overcoming the intrinsic E_g limitation of 2H-MoS_2 and enhancing its NIR response capability are crucial for improving its practical applicability.

In recent years, many studies have shown that introducing atomic-scale defects, such as sulfur vacancies (V_S), grain boundaries, or dislocations, during the preparation of MoS_2 can effectively modify the band structure and

---

[1] *School of Materials Science and Engineering, Fujian University of Technology, Fuzhou, Fujian, 350118, China*
[2] *School of Materials Science and Engineering, Xiamen University of Technology, Xiamen, Fujian, 361024, China*
[3] *Xiamen Tungsten Co., LTD, Xiamen, Fujian, 361001, China*

introduce defect energy levels, thereby optimizing carrier separation behavior and enhancing light-matter interactions, ultimately improving its optical properties.[9] Additionally, the ion doping strategy not only preserves the regulation effect of defects but also introduces unique electronic transitions, further broadening the light absorption range and promoting carrier separation. Rare earth element doping can introduce new energy levels within the E_g of intrinsic materials. These levels can effectively capture photons, enhance the generation efficiency of photogenerated carriers, modify the electronic structure, and improve the optoelectronic properties of the intrinsic material. Therefore, due to their rich energy level structures and unique electronic properties, rare earth elements have become ideal dopants for optimizing the performance of optoelectronic materials.[10,11] For example, rare earth neodymium (Nd^{3+}) doping has been shown to significantly enhance the fluorescence properties of $SrTiO_3$ nanoparticles,[12] influence the light absorption characteristics of ZnO films,[13] and greatly increase the carrier concentration and mobility of CuO films.[14] Therefore, developing precise strategies for the synergistic regulation of defect engineering and doping is essential for improving the NIR optoelectronic performance of MoS_2.

The strategies for modulating the electronic structure of MoS_2 mainly include physical, chemical, and combined regulation methods.[15,16] Although physical regulation (such as through strain fields or electric fields) allows for non-destructive and reversible tuning, its effectiveness is limited by intrinsic material parameters (such as deformation potential and exciton binding energy). Chemical regulation, especially element doping, provides an effective approach for atomic-level precise modulation of the electronic structure by altering the material's atomic composition and chemical environment. Among various synthesis methods, the hydrothermal method has demonstrated unique potential in the controlled preparation of MoS_2 and its doped systems, due to its mild reaction conditions, environmental friendliness, and scalability. Although theoretical and experimental studies on rare earth-doped MoS_2 have made progress, systematic research on defect engineering in Nd-doped MoS_2 (Nd:MoS_2) prepared via the hydrothermal method, particularly its effects on carrier dynamics and nonlinear optical properties, remains limited. Therefore, achieving enhanced NLO performance and improving its application potential in optoelectronic devices through the regulation of MoS_2 defect structure combined with synergistic rare earth element doping still presents a significant challenge.

In this work, Nd:MoS_2 nanosheets were synthesized via a one-step hydrothermal method, and the synergistic regulation mechanism of V_S and Nd^{3+} doping on the defect structure, optical E_g, photoluminescence (PL), NLO properties, and photocarrier dynamics in Nd:MoS_2 nanosheets was systematically investigated. The results show that due to the presence of V_S, the optical E_g of the hydrothermally synthesized MoS_2 nanosheets is significantly reduced from the theoretical value of 1.28 eV to 0.75 eV. After Nd^{3+} doping, the optical E_g of the Nd:MoS_2 nanosheets is further narrowed to 0.45 eV, effectively extending the light response and operational wavelength range of Nd:MoS_2. PL measurements indicate that the emission intensity of the Nd:MoS_2 nanosheets is twice that of the undoped MoS_2. Under a wavelength of 532 nm, open-aperture (OA) Z-scan tests reveal that both MoS_2 and Nd:MoS_2 nanosheets exhibit an intensity-dependent transition in nonlinear absorption (NLA) from saturable absorption (SA) to reverse saturable absorption (RSA), with Nd^{3+} doping significantly enhancing the RSA effect. The integration of femtosecond transient absorption spectroscopy and first-principles (DFT) calculations demonstrates that the synergistic coupling between the discrete energy levels introduced by Nd^{3+} and the V_S defect states shortens the carrier trapping time (τ_1) to 1.2 ps and prolongs the non-radiative recombination lifetime (τ_2) to 84.8 ps. This synergistic effect governs the transition of the NLA mechanism from ground-state absorption to excited-state absorption (ESA), while specifically promoting RSA effects in the NIR spectral region. This study demonstrates that Nd^{3+} doped Nd:MoS_2 nanosheets exhibit promising potential for NIR optoelectronic applications, including ultrafast lasers (SA), optical limiters (RSA), all-optical switches (SA/RSA switching), and phase modulators.

2. Experimental methods

2.1 Materials

High-purity (99.9% purity) chemicals, such as molybdenum trioxide (MoO_3), thiourea (CH_4N_2S), thioacetamide (C_2H_4NS), urea ($CO(NH_2)_2$), and ethanol (C_2H_5OH), were purchased from Aladdin. All reagents were of analytical grade and used without further purification.

2.2 Synthesis of MoS_2 nanosheets

3.4 g MoO_3, 2.4 g C_2H_4NS, 0.6 g CH_4N_2S, and 2 g urea were dissolved in 80 mL deionized water and stirred for 1 h to obtain mixed solution W_1. The mixed solution was then transferred to a 100 mL stainless steel autoclave liner and subjected to hydrothermal treatment at 200°C for 12 h. After natural cooling for 4 h, the precipitate was collected and

---

[4]*Équipe de Recherche sur les Processus Innovatifs (ERPI), Université de Lorraine, Nancy, 54000, France*

[#]*These authors contributed equally to this work*

[*]*Email:* cuizhixiang2006@126.com (Zhixiang Cui), sijunhui2004@126.com (Junhui Si)

centrifugally washed three times each with deionized water and anhydrous ethanol (using a fixed 8000 rpm speed to avoid vacancy differences caused by centrifugation) to remove surface impurities and adsorbed ions. Finally, freeze-drying was performed to obtain MoS_2 nanosheet powder with uniform particle size.

2.3 Synthesis of Nd:MoS_2 nanosheets

To the prepared W_1 solution from Section 2.2, 0.005 g of $NdCl_3$ was added and stirred at room temperature for 1 h. The mixture was then transferred to a 100 mL stainless steel autoclave liner and subjected to hydrothermal treatment at 200 °C for 12 h. After natural cooling for 4 h, the precipitate was collected. Finally, Nd:MoS_2 nanosheet powder was obtained through centrifugation, washing, purification, and freeze-drying. The preparation flowcharts for both MoS_2 and Nd:MoS_2 nanosheet powders are shown in Fig. S1.

2.4 Characterizations

The morphology and structure of the samples were analyzed using field emission scanning electron microscopy (SEM, S-3400N, Japan), atomic force microscopy (BRUKER, HARI-200-10), and transmission electron microscopy (TEM, Tecnai 12). The chemical composition of the samples was analyzed using an X-ray diffractometer (XRD, D8 ADVANCE, Bruker, Germany) and an InVia Reflex Raman spectrometer. The UV-visible absorption spectra of the samples were measured using a UV-visible spectrophotometer (UV-1800, Japan). PL intensity was tested using a fluorescence spectrometer (FL980). NLO properties of the samples were observed using a PL2250 picosecond laser, Nd:YAG laser system. Samples were dissolved in N,N-dimethylformamide solution and injected into a 2 mm path length quartz cuvette. Laser wavelengths used were 532 nm (sample transmittance 43%) and 1064 nm (sample transmittance 67%), with a pulse width of 30 ps, a beam waist radius of 23 mm, a Rayleigh length of 3.12 mm, and an excitation frequency of 10 Hz. A femtosecond laser (≈400 nm,≈3.1 eV photon energy) was used as the pump beam, and white light as the probe beam to measure transient absorption spectra.

3. Results and discussion

Fig. 1(a) shows the atomic models of Nd:MoS_2 nanosheets containing Vs and Nd^{3+} doping prepared by hydrothermal method from different angles. SEM images reveal that MoS_2 consists of nanosheets assembled into a flower-like structure (Fig. 1b and 1c), while Nd:MoS_2 forms a spherical structure composed of nanosheets (Fig. 1d and 1e),[17] which is attributed to the alteration of the assembly structure of layered MoS_2 nanosheets due to rare earth Nd^{3+} doping. Energy Dispersive X-ray Analysis (EDX) shows that MoS_2 nanosheets contained approximately 2% V_S (Fig. S2a), whereas Nd:MoS_2 nanosheets not only retain a similar V_S concentration (~2%) but also successfully incorporate 2% Nd^{3+} doping (Fig. S2b). The atomic force microscope (AFM) shows that the radius of MoS_2 and Nd:MoS_2 nanosheets is approximately 200 nm (Fig. S3a and Fig. S3b). The thickness profile diagram indicates that the thickness of the nanosheets is approximately 2.4 nm (Fig. S3c and Fig. S3d), suggesting that the number of layers of MoS_2 and Nd:MoS_2 nanosheets is approximately 4 layers.

Fig. 2 presents the TEM images of MoS_2 and Nd:MoS_2

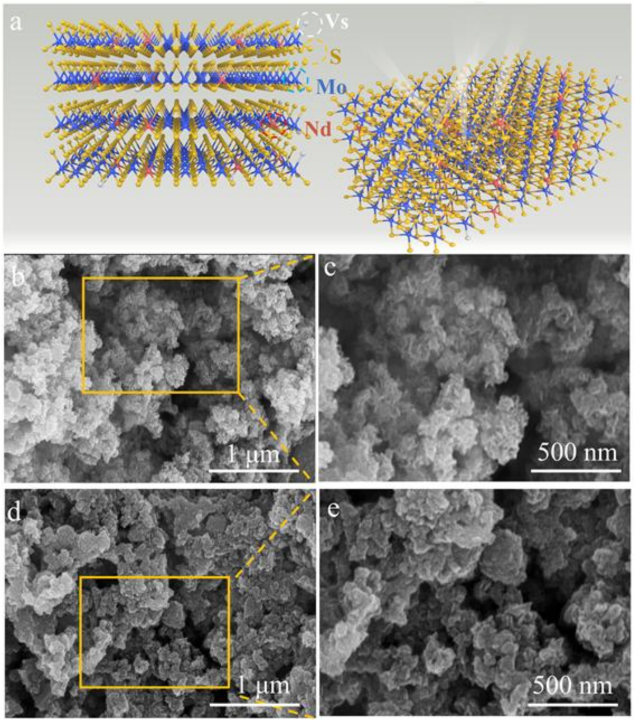

Fig. 1: (a) Schematic atomic configurations of the Nd:MoS_2 crystal structure from different angles. (b, c) SEM images of MoS_2 nanosheets with different magnification. (d, e) SEM images of Nd:MoS_2 nanosheets with different magnification.

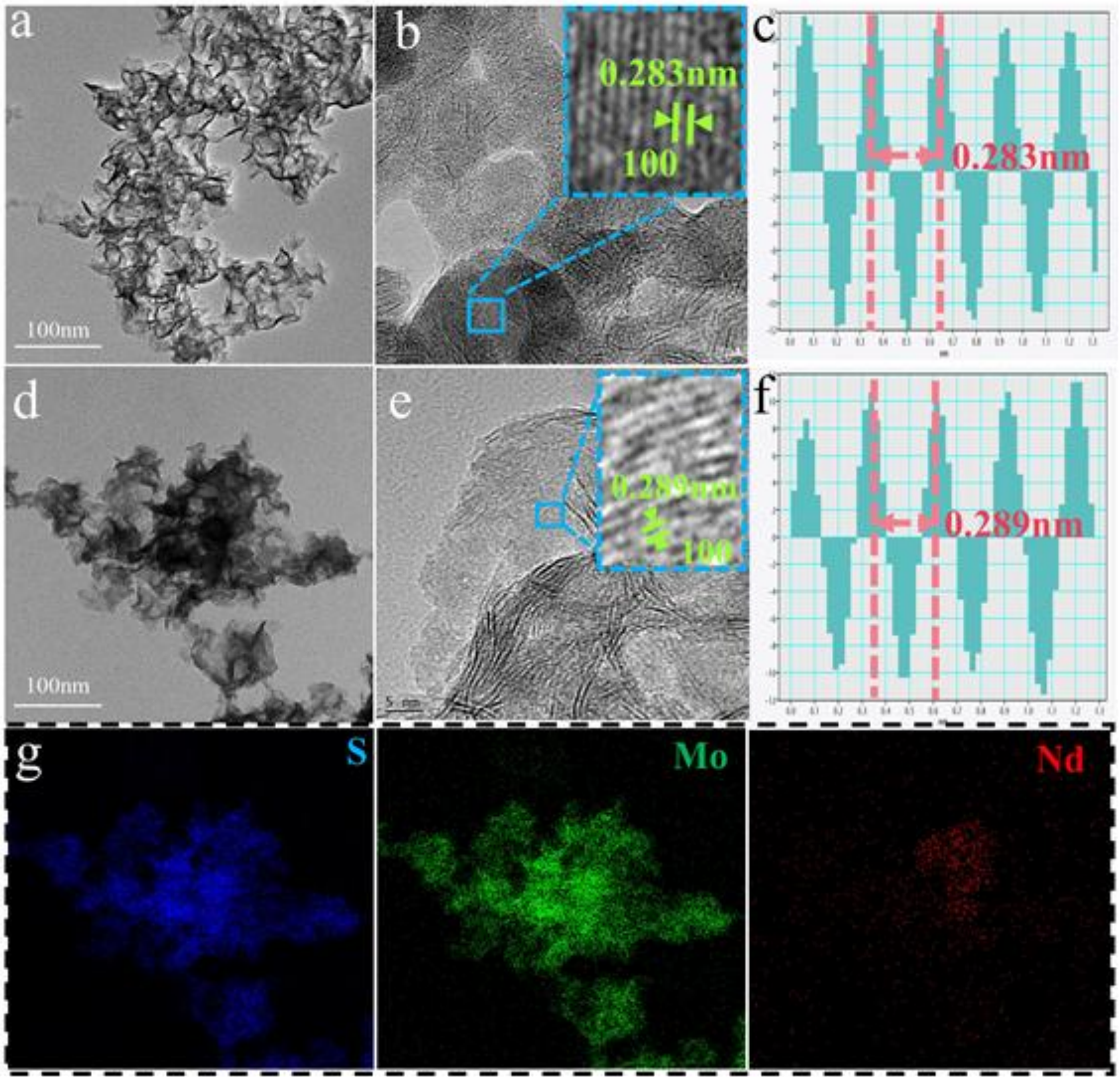

Fig. 2: (a, b) TEM and HRTEM images of MoS_2 nanosheets, with the blue box indicating a magnified view of the lattice fringes. (c) Lattice fringe spacing diagram of MoS_2 nanosheets. (d, e) TEM and HRTEM images of Nd:MoS_2 nanosheets, with the blue box indicating a magnified view of the lattice fringes. (f) Lattice fringe spacing diagram of Nd:MoS_2 nanosheets. (g) EDS mapping of Mo, S, and Nd elements in the Nd:MoS_2 nanosheets corresponding to image (d).

nanosheets. As can be seen from Figs. 2(a-c), MoS_2 nanosheets exhibit a layered structure and have clear lattice fringes with a lattice spacing of approximately 0.283 nm, which corresponds to the (001) plane of MoS_2 nanosheets. From Figs. 2(d-f), it can be observed that the morphology of Nd:MoS_2 nanosheets has changed compared to that of MoS_2 nanosheets. However, Nd:MoS_2 still has clear lattice fringes, and the lattice spacing has increased to 0.289 nm. This may be due to the fact that the atomic radius of Nd is larger than that of Mo, and the doping causes lattice distortion, changing the average distance between adjacent atoms and thereby slightly expanding the entire crystal structure.[18] Energy Dispersive X-ray spectroscopy (EDS) spectroscopy analysis reveals that Mo, S, and Nd elements are uniformly distributed in the Nd:MoS_2 nanosheets, further confirming the successful doping of Nd ions (Fig. 2g). From the electron diffraction (SAED) patterns, both MoS_2 and Nd:MoS_2 nanosheets exhibit diffraction spots corresponding to the (110) and (100) crystal planes, indicating that both types of nanosheets possess excellent crystalline structures (Fig. S4a and S4b).

Fig. 3(a) shows the XRD diffraction patterns of MoS_2 and Nd:MoS_2 nanosheets. It can be seen that the characteristic peaks appear at 14.28°, 34.18° and 57.2°, corresponding to the (002), (100), and (110) crystal planes of MoS_2, respectively.[19,20] Among them, the (002) crystal plane belongs to the interlayer diffraction along the c-axis direction, reflecting the periodicity of the S-Mo-S layered stacking and their interlayer distance, indicating that the MoS_2 nanosheets possess a good layered structure. The (100) crystal plane is perpendicular to the c-axis and belongs to the a-b plane diffraction, showing the atomic arrangement within the MoS_2

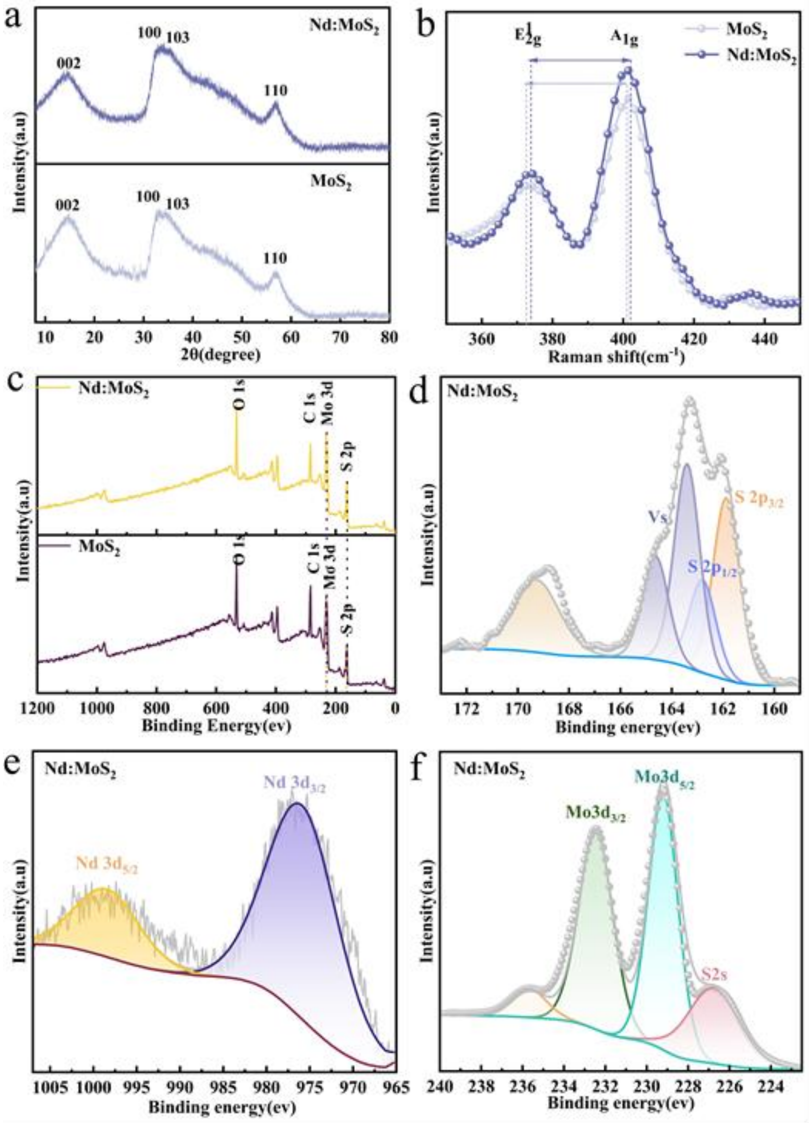

Fig. 3: (a) XRD diffraction patterns of MoS_2 and $Nd:MoS_2$ nanosheets. (b) Raman spectra of MoS_2 and $Nd:MoS_2$ nanosheets. (c) XPS survey spectra of MoS_2 and $Nd:MoS_2$ nanosheets. (d-f) High-resolution core-level XPS spectra of $Nd:MoS_2$ nanosheets: (d) S 2p orbital, (e) Nd 3d orbital, and (f) Mo 3d orbital.

monolayer, which is a repeating unit of S-Mo-S along the a-axis direction. This is consistent with the TEM and SEAD results (Fig. 2 and Fig. S4). Therefore, the 2H phase MoS_2 nanosheets with a hexagonal crystal structure were successfully synthesized by the hydrothermal method in this study. Compared with MoS_2 nanosheets, the XRD diffraction peaks of $Nd:MoS_2$ nanosheets do not show significant changes, indicating that the Nd^{3+} doping has not changed the crystal structure of MoS_2 nanosheets. The Nd atoms are present in MoS_2 nanosheets in a substitutional doping manner.[21] For the MoS_2 nanosheets, two typical characteristic peaks appear at 373.69 cm^{-1} and 400.47 cm^{-1}, corresponding to the E_{2g} and A_{1g} vibrations, respectively (Fig. 3b). Among them, the E_{2g} peak is due to the symmetric stretching vibration of the Mo-S bonds, that is, the Mo atom and S atom perform symmetric stretching movements within the a-b plane. The A_{1g} peak originates from the out-of-plane symmetric vibration of the S atoms (along the c-axis direction), that is, the two layers of S atoms move in opposite directions along the direction perpendicular to the a-b plane, while the Mo atoms remain stationary. These are characteristic peaks of the 2H phase MoS_2 in the hexagonal crystal structure.[22] Compared to MoS_2 nanosheets, the $Nd:MoS_2$ nanosheets exhibit E_{2g} and A_{1g} vibrational peaks at 373.76 cm^{-1} and 401.03 cm^{-1}, respectively, showing a redshift phenomenon. This is attributed to p-type doping occurring during the growth of $Nd:MoS_2$. Due to the similar electronegativity and small difference in atomic radius between Mo and Nd, Nd tends to substitute for Mo in the lattice. Since Nd ions are cations and MoS_2 itself is an n-type semiconductor (with free electrons in the conduction band), the doping of Nd^{3+} introduces holes (*i.e.*, positive charge carriers), thereby shifting the Fermi level downward toward the top of the valence band. This change imparts p-type doping characteristics to the material, induces lattice distortion in the hexagonal structure, and increases the carrier concentration due to hole injection. Here, S^{2-} acts as an acceptor, while the donor Nd^{3+} induces tensile stress, reducing electron-phonon scattering. In summary, Nd^{3+} doping causes charge and strain changes in Nd:MoS_2 nanosheets, leading to the redshift phenomenon. This result is consistent with previous studies on p-type doping via Nb doping in MoS_2.[23]

Fig. 3(c-f) and Fig. S5 present the XPS spectra of MoS_2 and Nd:MoS_2 nanosheets. In the S core-level spectra of both MoS_2 and Nd:MoS_2 nanosheets (Fig. 3d, Fig. S5a,), characteristic peaks are observed at approximately 163.52 eV and 164.8 eV, corresponding to bridging disulfide-type sulfur (S_2^{2-}) or unsaturated V_S, further confirming the presence of V_S in both materials.[23] In addition, the S 2p spectrum of MoS_2 exhibits a doublet at 161.97 eV (S $2p_{3/2}$) and 163.1 eV (S $2p_{1/2}$), which is attributed to the S^{2-} species in the basal plane of MoS_2. Notably, the S 2p characteristic peaks (S $2p_{3/2}$ and S $2p_{1/2}$) of Nd:MoS_2 nanosheets shift toward lower binding energies compared to those of pure MoS_2 (Table S1). Similarly, the XPS spectrum of Nd:MoS_2 (Fig. 3e) clearly shows Nd characteristic peaks at 975.86 eV and 998.43 eV, further confirming the successful doping of Nd^{3+}. Fig. 3(f) and Fig. S5b show that the Mo 3d spectrum of MoS_2 exhibits characteristic peaks at 229.24 eV (Mo $3d_{5/2}$) and 232.65 eV (Mo $3d_{3/2}$), which are attributed to the Mo-S bonds, while the peak at 236.0 eV corresponds to the presence of a small amount of Mo^{6+} due to slight oxidation. Notably, the Mo 3d characteristic peaks (Mo $3d_{5/2}$ and Mo $3d_{3/2}$) of Nd:MoS_2 nanosheets also shift toward lower binding energies by approximately 0.1 eV (Table S1), which are attributed to the change in lattice spacing caused by Nd^{3+} doping. The above results indicate that the doping of Nd^{3+} causes shifts in the core-level spectral peaks of both S and Mo toward lower

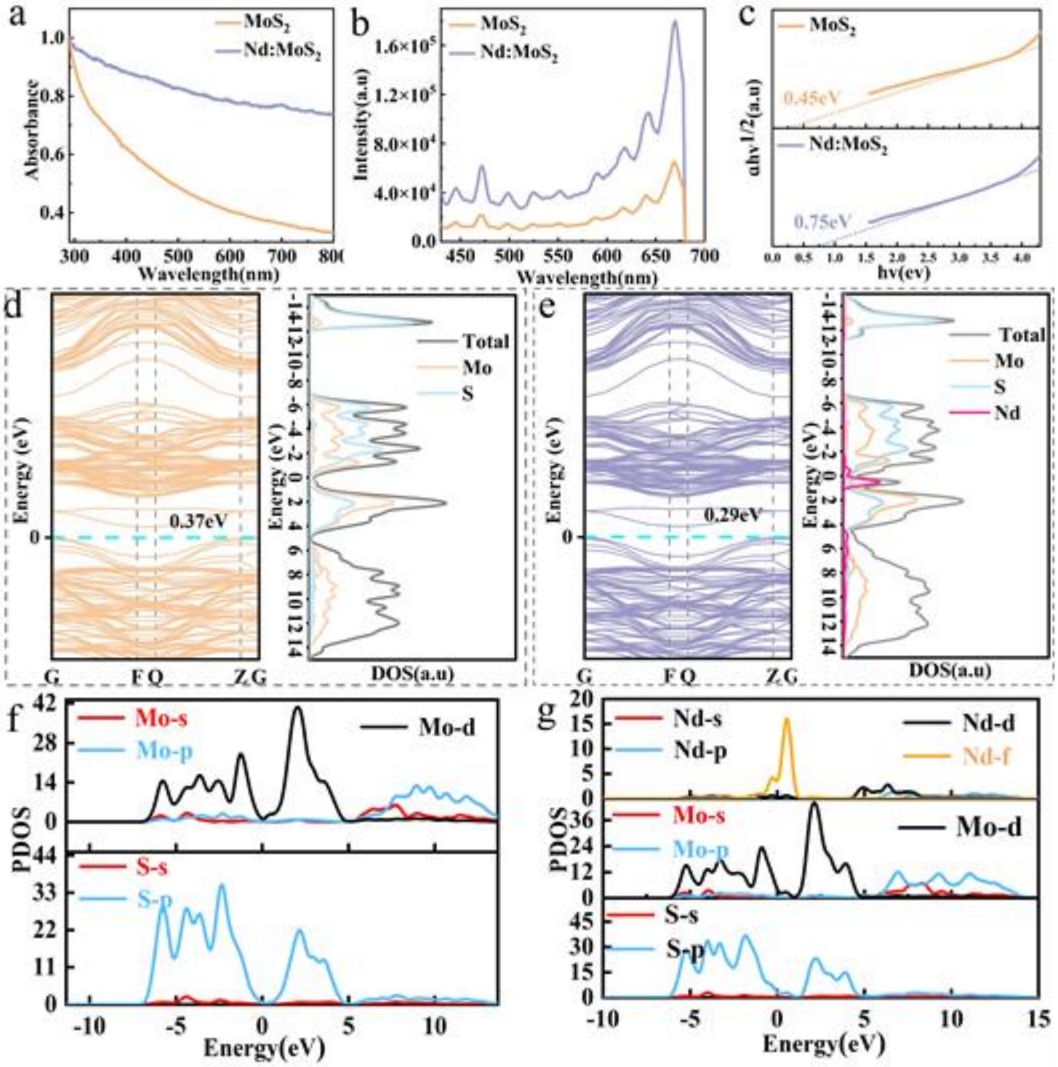

Fig. 4: (a) UV-Vis absorption spectra of MoS_2 and Nd:MoS_2 nanosheets. (b) PL intensity comparison of MoS_2 and Nd:MoS_2 nanosheets. (c) Tauc plots of MoS_2 and Nd:MoS_2 nanosheets. (d, e) projected band structures and density of states (DOS) of MoS_2 and Nd:MoS_2 nanosheets, respectively (with the Fermi level set to the top of the valence band). (f) and (g) are the Projected Density of States (PDOS) of MoS_2 and Nd:MoS_2 nanosheets, respectively.

binding energies, which may be attributed to the transition of the material from n-type to p-type conductivity induced by Nd^{3+} doping.[24]

Fig. 4(a) shows the UV-Vis absorption spectra of MoS_2 and Nd:MoS_2 nanosheets. Compared to MoS_2, Nd:MoS_2 exhibits significantly enhanced background absorption across the entire spectral range. This enhancement may arise from two factors: on one hand, the introduction of Nd^{3+} during the hydrothermal synthesis may cause distortions in the octahedral crystal field, thereby perturbing the structural continuity of the 2D nanosheets (approximately 200×200 nm in size), which could contribute additional light scattering at the Rayleigh scattering scale; on the other hand, the new electronic energy levels introduced by Nd^{3+} may increase the carrier concentration, thereby enhancing the overall light absorption capability of Nd:MoS_2,[25] which is consistent with the observations from Raman spectroscopy. Fig. 4b displays the room-temperature PL spectra of MoS_2 and Nd:MoS_2 nanosheets measured using a 365 nm laser as the excitation source. The PL intensity of the Nd:MoS_2 nanosheets is significantly enhanced compared to MoS_2, with an enhancement factor approaching twice. This indicates that the doping Nd^{3+} effectively improves the light absorption efficiency and radiative recombination efficiency of MoS_2 nanosheets. The energy levels introduced by Nd^{3+} can serve as efficient excitation active centers, effectively capturing excitation energy and promoting photon emission through radiative recombination, thereby significantly enhancing the overall luminescent performance of the material. Specifically, Nd^{3+} doping introduces its characteristic 4f energy levels within the bandgap of MoS_2. Upon light absorption by the MoS_2 matrix, the energy is transferred non-radiatively via resonant energy transfer to the Nd^{3+} ions, which then release the energy in the form of their characteristic radiation. This provides a novel and highly efficient pathway for PL enhancement.[26] The indirect E_g of the material was calculated using the Tauc formula as following Eq. (1).[27]

$$(\alpha h\nu)^n = A(h\nu - E_g) \tag{1}$$

here, A is a constant, h is Planck's constant, v is the frequency, and α is a proportionality constant. For indirect bandgap semiconductors (such as MoS2 and Nd:MoS2 nanosheets), n is taken as 1/2 for the indirect bandgap. The calculation results (Fig. 4c) showed that Nd3+ doping reduces Eg from≈0.75 eV in MoS2 to≈0.45 eV in Nd:MoS2. It should be noted that the Eg of standard defect-free 2H-phase four-layer MoS2 is approximately 1.28 eV. The Eg of the undoped MoS2 nanosheets in this study (≈0.75 eV) is significantly lower than this value, which is most likely attributed to Vs introduced during the hydrothermal synthesis process. Here, VS typically act as shallow donors or deep-level traps, which can introduce defect states within the Eg. The presence of defect states may cause electrons originally belonging to the conduction band to become localized, thereby reducing the effective Eg of the material.

To further investigate the effects of Vs and Nd^{3+} doping on the electronic structure of MoS_2, the DFT calculations was performed. Fig. S6 displays the theoretically calculated models for crystal structures of the defect-free MoS_2, MoS_2 with S vacancies MoS_2 with both S vacancies and Nd^{3+} doping. The band structure analysis of Vs-containing MoS_2 nanosheets (Fig. 4d) revealed that the introduction of Vs significantly modifies the conduction band (CB) and valence band (VB) edges of MoS_2, generating new defect levels between the conduction band minimum (CBM) and the Fermi level. This results in a reduction of the theoretically calculated E_g from 1.3 eV in the defect-free system (Fig. S7a) to≈0.37 eV in the Vs-containing system. When Nd^{3+} is further doped into Vs-containing MoS_2 (Fig. 4e), the theoretically calculated E_g decreases further to≈0.29 eV, accompanied by the emergence of new energy levels. It should be noted that the theoretically calculated E_g values (0.37 eV and 0.29 eV) are systematically lower than the experimental values (0.75 eV and 0.45 eV), respectively. This discrepancy primarily arises from the systematic underestimation of semiconductor E_g inherent to the generalized gradient approximation (PBE) functional employed in the calculations.[28] Furthermore, density of states (DOS) calculations (Fig. 4e) reveal that Nd^{3+} doping introduces additional electronic states. These states may participate in accommodating photogenerated electrons, thereby enhancing the light absorption process. Compared to defect-free MoS_2 (Fig. S7b), the Projected Density of States (PDOS) of MoS_2 with V_S (Fig. 4f) exhibits new electronic states near the Fermi level (-2 eV to 2 eV). These states arise from the reconstruction of dangling bonds on adjacent Mo atoms induced by S vacancies, resulting in localized defect states appearing near the Fermi level. After doping with Nd^{3+} (Fig. 4g), new electronic states are introduced, among which the Nd-4f orbitals exhibit sharp and intense peaks in the middle of the band gap (-2 eV to 2 eV), forming strongly localized deep-level states. Furthermore, the spectra clearly show overlapping peak positions and correlated shapes between the density of states of Nd-4f, Mo-d, and S-p orbitals, confirming orbital hybridization among them. This hybridization establishes novel hybrid molecular orbitals, providing additional optical transition pathways and thereby effectively modulating the material's optical properties. The DFT calculation results provided theoretical support for the

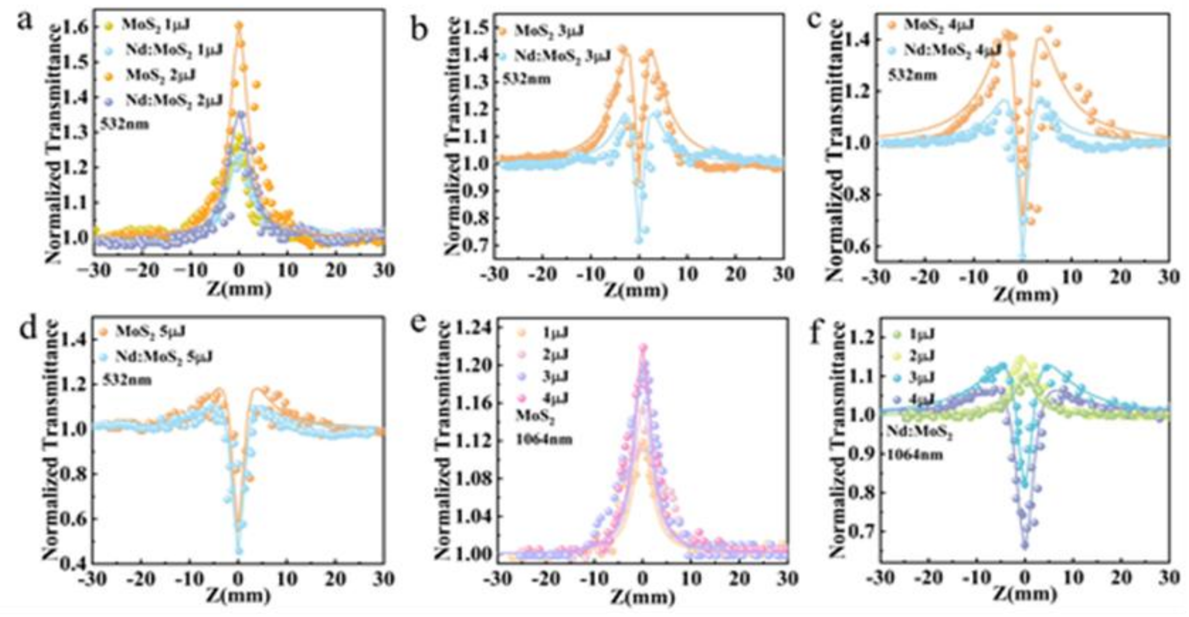

Fig. 5: (a-d) OA Z-scan curves of MoS_2 and Nd:MoS_2 nanosheets under excitation wavelength of 532 nm with pulse energies ranging from 1 μJ to 5 μJ. (e, f) OA Z-scan curves of MoS_2 and Nd:MoS_2 nanosheets under excitation wavelength of 1064 nm with pulse energies ranging from 1 μJ to 4 μJ. (the data points represent experimental results, and the solid lines are fitting curves based on the experimental data using a model).

experimentally observed enhancement in both light absorption and PL intensity through Nd^{3+} doping.[29]

This study systematically investigated the broadband NLA properties of MoS_2 and Nd:MoS_2 nanosheets using OA Z-scan technique at wavelengths of 532 nm and 1064 nm. This technique analyzes NLA by moving the sample (or focal point) along the direction of beam propagation (the optical axis) and recording the changes in the light intensity through the sample. The normalized transmittance (defined as the ratio of nonlinear transmittance to linear transmittance) is a key parameter for evaluating the NLA performance of materials. In NLA measurements, the SA effect is characterized by an increase in normalized transmittance with increasing incident light intensity (pump intensity), whereas the RSA effect is characterized by a decrease in normalized transmittance with increasing incident light intensity. A schematic diagram of the picosecond laser system used for the measurements is shown in Fig. S8. To ensure that the observed NLA signal was entirely derived from the sample itself and not from the solvent, we conducted Z-scan tests on pure solvents under different laser energies. The results indicated that the solvent did not exhibit any detectable nonlinear optical response under any of the tested energies, thereby confirming that the NLA properties of the sample were indeed caused by the nanosheet material and are not attributable to thermal effects from the solvent. It is worth noting that the nonlinear processes occurring under strong laser irradiation may lead to temperature rise in the samples, which could potentially induce the formation of scattering centers. According to the study by Aleali *et al*,[30] the effective scattering coefficient (γ_S) can be described by the Rayleigh-Gans relation. The calculated γ_S values for MoS_2 and Nd:MoS_2 nanosheets are 7.35×10^{-29} cm^3/W^2 and 1.09×10^{-28} cm^3/W^2, respectively (Tables S2 and S3,). Compared to the γ_S value of silver nanoparticles reported by Aleali *et al*. ($7.5 \times 10^{-18} cm^3/W^2$), the γ_S values in this study are approximately 10^{-11} times lower. Given the extremely weak scattering effect, its influence was neglected in the subsequent Z-scan data analysis.

Fig. 5(a) presents the Z-scan curves of MoS_2 and Nd:MoS_2 nanosheets at 532 nm with pulse energies of 1 μJ and 2 μJ. At 1 μJ, both samples exhibit a significant SA effect. This primarily arises because the photon energy ($h\nu$≈2.33 eV) exceeds the E_g of the samples (E_g≈0.75 eV and 0.45 eV), enabling the excitation of VB electrons to fill the CB energy levels. According to the Pauli exclusion principle, when the excited states are occupied by electrons to a certain extent, the ground-state absorption becomes saturated, leading to the SA effect. As the laser energy increases to 2 μJ, the SA modulation amplitude at the focal point is further enhanced. Figures 5(b-d) show the Z-scan curves at 532 nm with energies of 3 μJ, 4 μJ, and 5 μJ. When the energy increases to 3 μJ, the SA effect of MoS_2 and Nd: MoS_2 weakens. The normalized transmittance curves of these materials are greater than 1 away from the focus in the low light intensity zone, while they are less than 1 near the focus in the high light intensity zone, showing a first peak then valley characteristic, indicating that the NLA behavior changes from SA to RSA. When the energy is further increased to 4 μJ and 5 μJ, the normalized transmittance in the focal region further decreases. The SA effect continues to weaken while the RSA effect significantly strengthens. Moreover, Nd:MoS_2 exhibits stronger RSA characteristics than MoS_2. The mechanism of RSA may include nonlinear scattering, ESA, or two-photon absorption (TPA) *et al*. Under the experimental conditions of this study, the laser pulse width exceeds the actual carrier relaxation time. This conclusion is verified by subsequent carrier lifetime measurements in Fig. 10, thus the singlet excited state plays a dominant role.[31] The SA effect relies on the transition from the ground state to the first excited state, while the RSA effect depends on the transition from the first excited state to higher excited states (ESA). SA occurs because the ground-state absorption cross-section is larger than the excited-state absorption cross-section, whereas RSA arises when the excited-state absorption cross-section exceeds that of the ground state. Therefore, the transition from SA to RSA can be attributed to the competition between ground-state and excited-state absorption cross-sections as a function of light intensity.

Fig. 5(e) shows the Z-scan curves of MoS_2 nanosheets at 1064 nm with pulse energies ranging from 1 μJ to 4 μJ. The MoS_2 nanosheets exhibit SA behavior under all tested energy levels. Notably, at 1064 nm (photon energy≈1.16 eV), the incident photon energy is lower than the E_g of the standard 2H-phase MoS_2 (E_g≈1.28 eV), which theoretically does not satisfy the ground-state absorption condition $E_g < h\nu$. However, in this study, the as-prepared MoS_2 nanosheets exhibit a SA response in the infrared region. This is because the actual E_g is significantly reduced due to Vs and edge defects generated during the hydrothermal synthesis process (experimentally measured E_g≈0.75 eV, DFT calculations yielded E_g≈0.37 eV).[32] These defects introduce mid-gap states that enable sub-E_g photon absorption (defect-assisted absorption). Fig. 5(f) shows the Z-scan curves of Nd:MoS_2 nanosheets at 1064 nm with pulse energies ranging from 1 μJ to 4 μJ. At energies between 1 and 2 μJ, Nd:MoS_2 exhibits SA behavior similar to that of pure MoS_2. However, when the energy is increased to 3-4 μJ, the Nd:MoS_2 transitions from SA to RSA. This indicates that Nd^{3+} doping effectively modulates the NLA response of MoS_2 nanosheets, and introduces a new RSA behavior at higher light intensities.

Fig. 6 (a, b) show the relationship between output energy (Fout) and input energy (Fin) for MoS_2 and Nd:MoS_2 nanosheets under a laser wavelength of 532 nm. In the low-input-energy region, the Fout of both MoS_2 and Nd:MoS_2 nanosheets increases linearly with Fin, indicating that the slope of the Fin/Fout curve is greater than 1. This suggests that the normalized transmittance increases with increasing light intensity, which is a typical characteristic of SA effect. As the input energy increases, the trend of Fout increasing with Fin weakens, gradually transitioning to sub-linear growth, where the slope of the Fin/Fout curve becomes less than 1. This

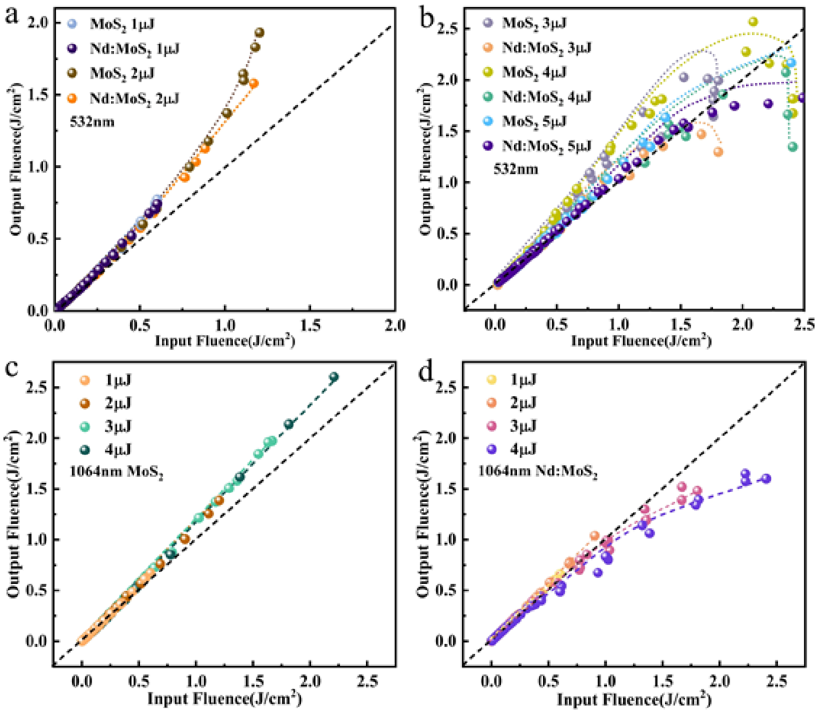

Fig. 6: (a, b) The relationship between output pulse energy and input pulse energy for MoS_2 and Nd:MoS_2 nanosheets under excitation at 532 nm with pulse energies ranging from 1 μJ to 5 μJ. (c, d) The relationship between output pulse energy and input pulse energy for MoS_2 and Nd:MoS_2 nanosheets under excitation at 1064 nm with pulse energies ranging from 1 μJ to 4 μJ. (Black dashed line: indicates a linear relationship between output and input pulse energy. colored dashed lines represent the fitting curves based on experimental data).

indicates that the normalized transmittance of the material decreases with increasing light intensity, corresponding to the RSA effect. Moreover, when the laser power is increased to higher input energies, the Fin/Fout curve no longer follows a linear relationship. This nonlinear dependence further confirms that MoS_2 and Nd:MoS_2 nanosheets exhibit significant NLA characteristics at 532 nm wavelength. Fig. 6 (c, d) show the variation of Fout with Fin for MoS_2 and Nd:MoS_2 nanosheets under a laser wavelength of 1064 nm. For the MoS_2 nanosheets, Fout increases linearly with Fin across the entire tested input energy range, indicating that the normalized transmittance monotonically increases with light intensity, showing only SA behavior. For the Nd:MoS_2 nanosheets, a similar linear increase is observed in the low-input-energy region, also indicating the presence of SA effect. However, as the input energy further increases, the growth trend of Fout with Fin weakens and transitions into sub-linear growth (Fin/Fout < 1), suggesting that the normalized transmittance starts to decrease with increasing light intensity, which corresponds to the emergence of RSA effect. These results demonstrate that Nd:MoS_2 nanosheets not only exhibit SA behavior but also possess RSA effect, revealing strong nonlinear optical response and excellent light-intensity-dependent optical signal modulation capability.

A NLA model incorporating both SA and RSA effects, as shown in Eq. (2),[33] was used to theoretically analyze the experimental Z-scan results.

$$\alpha(I) = \alpha_0/(I + I/I_S) \tag{2}$$

here, α_0 is the linear absorption coefficient, I is the laser intensity, β is the absorption coefficient, and I_S is the saturation intensity. Using Eq. (2), the corrected normalized transmittance can be expressed as Eq. (3)

$$T(Z) = Q(Z) / \left[\sqrt{\pi} q(Z)\right] \int ln[1 + q(Z) exp(-\tau_2) d\tau] \tag{3}$$

where

$$Q(Z) = exp[\alpha_0 L I / (I + I_S)]$$

$$q(Z) = \beta I_0 L_{eff} / \; (I + Z^2 / Z_0{}^2)$$

I_0 is the focused peak intensity, L_{eff} = [1-exp(-α_0L)]/α_0, where L_{eff} is the effective thickness of the sample and L is the actual sample thickness. $Z_0 = \pi\omega_0^2$, where Z_0 is the Rayleigh length and ω_0 is the beam waist radius. The imaginary part of the third-order nonlinear optical susceptibility, $Im\chi^{(3)}$, can be expressed by Eq. (4):[34]

$$Im\chi^{(3)} = (10^{-7} C\lambda n^2 / \alpha_0)\beta \tag{4}$$

here, C is the speed of light, λ is the wavelength of the incident light, and n is the refractive index. The Fig of merit (FOM) for nonlinear saturable absorption is defined by Eq. (5)

$$FOM = \left| Im\chi^{(3)} / \alpha_0 \right| \beta \tag{5}$$

The Z-scan curves fitted according to the above formula were used to determine the β and I_S of MoS_2 and Nd:MoS_2 nanosheets. The fitted saturation intensity I_S and nonlinear absorption coefficient β are shown in Table 1 and Table 2, respectively.

Table 1 presents the third-order nonlinear parameters of MoS_2 and Nd:MoS_2 nanosheets at a wavelength of 532 nm. It can be seen that, whether the NLA response exhibits SA or RSA behavior, Nd^{3+} doping significantly enhances the I_S of MoS_2 nanosheets at 532 nm.[25] To explain this phenomenon, a four-level energy transfer model (Fig. 7) based on the electronic structure's VB and CB was proposed for MoS_2 and Nd:MoS_2 nanosheets, supported by the DFT-calculated band structures (Fig. 4d and 4e). As shown in Fig. 7, the physical mechanism of the doping effect can be understood as the 4f electron orbitals of Nd^{3+} ions introducing new energy levels in

Table 1: The third-order nonlinear parameters of MoS_2 and Nd:MoS_2 nanosheets at a wavelength of 532 nm.

Laser	Samples	NLO response	β (cm GW^{-1})	I_S (GW cm^{-2})	$Im\chi^{(3)}$ (esu)	FOM (esu cm)
1μJ	MoS_2	SA	-10.5	8×10^2	-3.62×10^{-12}	8.58×10^{-13}
	Nd:MoS_2	SA	-9.2	5×10^3	-3.17×10^{-12}	7.51×10^{-13}
2μJ	MoS_2	SA	-8	7×10^4	-2.76×10^{-12}	6.54×10^{-13}
	Nd:MoS_2	SA	-6	1.7×10^5	-2.07×10^{-12}	4.91×10^{-13}
3μJ	MoS_2	RSA	5.4	0.48	1.86×10^{-12}	4.41×10^{-13}
	Nd:MoS_2	RSA	8	0.98	2.76×10^{-12}	6.54×10^{-13}
4μJ	MoS_2	RSA	7.4	0.31	2.55×10^{-12}	6.04×10^{-13}
	Nd:MoS_2	RSA	10	0.85	3.45×10^{-12}	8.18×10^{-13}
5μJ	MoS_2	RSA	8.5	0.89	2.93×10^{-12}	6.94×10^{-13}
	Nd:MoS_2	RSA	12	1.05	4.14×10^{-12}	9.81×10^{-13}

Table 2: The third-order nonlinear parameters of MoS_2 and $Nd{:}MoS_2$ nanosheets at a wavelength of 1064 nm.

Laser	Samples	NLO response	β (cm GW^{-1})	I_S (GW cm^{-2})	$Im\chi^{(3)}$ (esu)	FOM (esu cm)
1μJ	MoS_2	SA	-0.71	2×10^4	-4.90×10^{-13}	2.45×10^{-13}
	$Nd{:}MoS_2$	SA	-0.62	1×10^5	-4.28×10^{-13}	2.13×10^{-13}
2μJ	MoS_2	SA	-0.45	2.5×10^4	-3.10×10^{-13}	1.55×10^{-13}
	$Nd{:}MoS_2$	SA	-0.42	3×10^5	-2.90×10^{-13}	1.45×10^{-13}
3μJ	MoS_2	SA	-0.36	3.2×10^4	-2.48×10^{-13}	1.24×10^{-13}
	$Nd{:}MoS_2$	RSA	1.1	0.2	7.59×10^{-13}	3.79×10^{-13}
4μJ	MoS_2	SA	-0.29	4×10^4	-2.00×10^{-13}	9.99×10^{-14}
	$Nd{:}MoS_2$	RSA	1.4	0.35	9.66×10^{-13}	4.82×10^{-13}

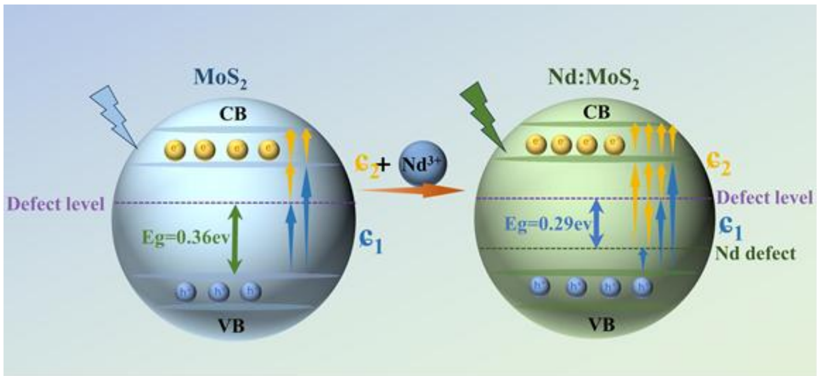

Fig. 7: Schematic of carrier dynamics in MoS_2 and $Nd{:}MoS_2$ nanosheets.

the band gap of MoS_2, significantly altering its electronic structure. These new energy levels provide additional electron transition pathways. The Raman spectroscopy results (discussed earlier) indicate that Nd3+ dopes MoS2 in a p-type manner, increasing the hole concentration (carrier concentration) in the material.[23] A higher carrier concentration means more energy is required to excite an equivalent proportion of carriers, which may be one of the reasons why the doped samples exhibit a higher I_S. Additionally, when the NLA response exhibits RSA behavior (at high energy levels), Nd^{3+} doping also significantly enhances the NLA coefficient β of the material. For instance, at an excitation energy of 4 μJ, the NLA coefficient β of MoS_2 nanosheets is 7.4 cm GW^{-1}, whereas that of $Nd{:}MoS_2$ increases to 10 cm GW^{-1}. At an excitation energy of 5 μJ, the β of MoS_2 reaches 8.5 cm GW^{-1}, while that of $Nd{:}MoS_2$ increases to 12 cm GW^{-1}. These results indicate that Nd^{3+} doping effectively enhances the RSA capability of the material under high light intensity.

Table 2 presents the third-order nonlinear parameters of MoS_2 and $Nd{:}MoS_2$ nanosheets at a wavelength of 1064 nm. As shown in Table 2, at 1064 nm and under excitation energies of 1 μJ and 2 μJ, both MoS_2 and $Nd{:}MoS_2$ nanosheets exhibit SA behavior in their NLA response. For instance, at 1 μJ, the I_S of MoS_2 is 2×10^4 GW cm^{-2}, while that of Nd: MoS_2 increases to 1×10^5 GW cm^{-2}, an increase of approximately five times. at 2 μJ, the I_S of MoS_2 is 2.5×10^4 GW cm^{-2}, while that of $Nd{:}MoS_2$ increases to 3×10^5 GW cm^{-2}, an increase of approximately twelve times. This is consistent with the observations at 532 nm, further demonstrating the role of doping in enhancing the saturation threshold. Moreover, When the excitation energy increases to 3 μJ and 4 μJ, the NLA response of MoS_2 still exhibits an SA behavior, while that of $Nd{:}MoS_2$ transitions to an RSA behavior. The persistent SA effect in MoS_2 is attributed to its ground-state absorption cross-section ($ɕ_1$) being larger than its excited-state absorption cross-section ($ɕ_2$).[34] The RSA effect observed in $Nd{:}MoS_2$ is attributed to the discrete energy levels introduced by Nd^{3+} doping, which significantly increase the excited-state absorption cross-section $ɕ_2$, resulting in $ɕ_2 > ɕ_1$. These discrete energy levels provide efficient pathways for ESA, thereby enhancing the probability of ESA occurrence. Consequently, ESA dominates the NLA response under high light intensity, leading to the transition from SA to RSA. This mechanism will be further verified in subsequent sections in combination with more in-depth spectroscopic characterization, such as transient absorption spectroscopy. The above results demonstrate that Nd^{3+} doping can significantly enhances the I_S of $Nd{:}MoS_2$ nanosheets, improving their anti-saturation capability. At 532 nm and under high light intensity, it increases the NLA coefficient β and strengthens the RSA effect. At 1064 nm and under high light intensity, it induces a transition in the NLA response from SA to RSA. This demonstrates the effective regulation and significant enhancement of the nonlinear optical absorption capacity of Nd:MoS_2 nanosheets by Nd^{3+} doping. To verify the four-level model for the NLA mechanism and to reveal the principle by which Nd^{3+} energy levels alter the NLO mechanism, the ɕ_1 and ɕ_2 absorption cross-sections of MoS_2 and Nd:MoS_2 at 3μJ were calculated using Eq. (6) and (7).[25]

$$\text{ɕ}_1 = -logT_0 / (NL) \tag{6}$$

$$\text{ɕ}_2 = -logT_{max} / (NL) \tag{7}$$

Here, T_0, T_{max}, N, and L represent the transmittance in the low-intensity linear regime, the high-intensity saturated transmittance, the ground-state carrier density, and the thickness of the MoS_2 and Nd:MoS_2 samples (~2.4 nm). The calculated values of ɕ_2 and ɕ_1 for Nd:MoS_2 are 8.13×10^{-13} cm^2 and 2×10^{-12} cm^2. The values of ɕ_2 and ɕ_1 for MoS_2 are 2.30×10^{-13} cm^2 and 1.54×10^{-13} cm^2. Based on these calculated absorption cross-sections, the ɕ_2/ ɕ_1 ratios are 1.49 and 0.41 for Nd:MoS_2 and MoS_2, respectively, further indicating that Nd^{3+} doping significantly enhances the excited-state absorption cross-section by introducing new energy levels within the excited states of MoS_2.

Fig. 8 presents the relationship between the normalized transmittance of MoS_2 and Nd:MoS_2 nanosheets and the input laser pulse energy. As shown in Figs. 8(a, b), in the visible light region (532 nm), when the input energy is lower (1 μJ and 2 μJ), the normalized transmittance of MoS_2 and Nd:MoS_2 nanosheets both increase with the increase of input energy and gradually deviate from the linear response, showing obvious SA characteristics. This indicates that both MoS_2 and Nd:MoS_2 nanosheets have the potential to be used as saturable absorbers at 532 nm wavelengths, applicable in devices such as mode-locked lasers, Q-switches, and optical switches/modulators. However, when the input energy increases to 3 μJ, 4 μJ, and 5 μJ, the normalized transmittance of MoS_2 and Nd:MoS_2 nanosheets shows a trend of first increasing (dominated by SA) and then decreasing (dominated by RSA). This indicates that the nonlinear absorption behavior of the materials has undergone a transition from SA to RSA. Notably, in the near-infrared region (1064 nm) (Figs. 8c and 8d), as the input energy increases from low to high (1-4 μJ), MoS_2 exhibits SA characteristics, while Nd:MoS_2 shows SA characteristics at low input energies and transforms into RSA characteristics at high input energies. Therefore, the results indicate that due to the doping of Nd^{3+}, the controllable transformation from SA to RSA of Nd:MoS_2 nanosheets has expanded from the visible light region to the near-infrared region. The existence of RSA effect enables the material to show application prospects in optical limiters and laser pulse shaping, while the SA-RSA transformation shows application prospects in various optical devices, such as fast optical

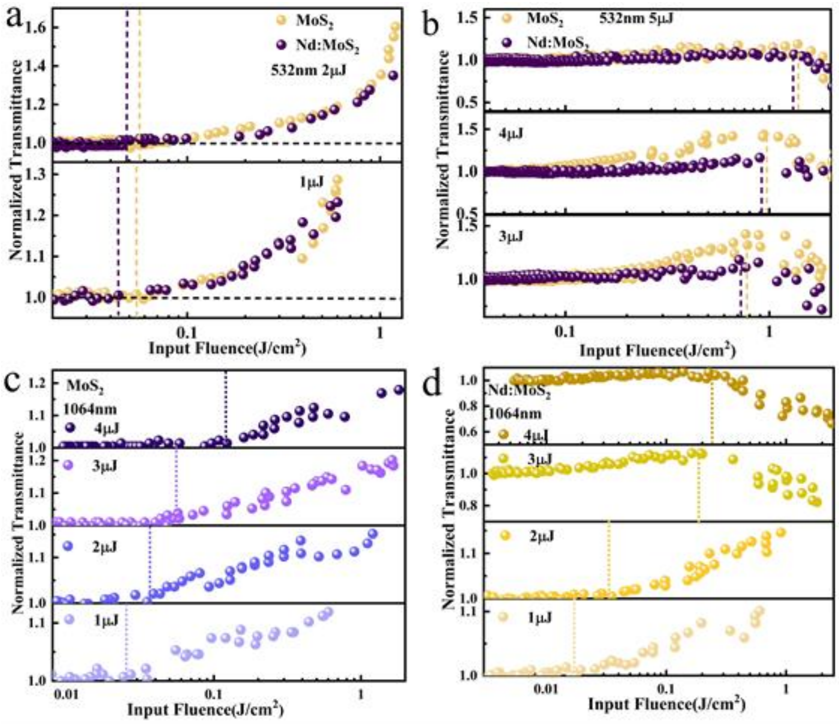

Fig. 8: (a, b) Relationship between the normalized transmittance and input pulse energy for MoS_2 and Nd:MoS_2 nanosheets under excitation at 532 nm with excitation energies ranging from 1 μJ to 5 μJ. (c, d) Relationship between the normalized transmittance and input pulse energy for MoS_2 and Nd:MoS_2 nanosheets under excitation at 1064 nm with excitation energies ranging from 1 μJ to 4 μJ. (Dashed lines: Onset points of SA and RSA for MoS_2 and Nd:MoS_2 nanosheets).

switches, optical limiters, optical bistable devices, and even all-optical logic gates that require dynamic optical control functions.[31,35] Additionally, the onset threshold is a key parameter characterizing SA and RSA properties, defining the critical light intensity at which a material transitions from linear absorption to significant NLA behavior (SA or RSA). For SA applications, a lower SA onset threshold generally indicates that the device can achieve its functionality (*e.g.*, initiating mode-locking) at lower operating light intensities, making it one of the important metrics for evaluating performance quality.[36] The above results indicate that, although when the MoS_2 and $Nd{:}MoS_2$ nanosheets are within the same type of NLA response range, the $Nd{:}MoS_2$ always exhibit a lower SA starting threshold than the MoS_2. This further confirms that Nd^{3+} doping effectively reduces the saturation threshold of the material, thereby enhancing its performance as a saturable absorber. It is worth noting that at 1064 nm and under excitation energies of 3-4 μJ, MoS_2 nanosheets exhibit SA behavior, while $Nd{:}MoS_2$ nanosheets exhibit RSA behavior. Since the two materials are governed by different NLA mechanisms at this stage, the corresponding critical threshold parameters (SA saturation threshold vs. RSA initial threshold) are not physically comparable. Therefore, no threshold comparison was made at this energy point.

The third-order nonlinear refraction (NLR) properties of MoS_2 and $Nd{:}MoS_2$ nanosheets were investigated using the closed-aperture (CA) Z-scan technique. The experimental data were fitted based on the standard theoretical Eq. (8)[37]

$$T_n = 1 + 8[(Z/Z_0)/(1 + (Z/Z_0)^2(9 + (Z/Z_0)^2)]n_2 E_{in} L_{eff} / (\omega_0 \lambda \pi) \tag{8}$$

here, T_n is the normalized transmittance, Z/Z_0 is the normalized position of the sample, which determines the positions and shapes of the peaks and valleys in the curve, E_{in} is the energy of the incident laser pulse, and n_2 is the nonlinear refractive index coefficient. Under excitation at a wavelength of 532 nm with an incident energy of 3 μJ, the fitting results indicate that the n_2 value for MoS_2 nanosheets is -0.8×10^{-12} m^2/W. The CA Z-scan curve (Fig. 9a) shows a maximum transmittance (peak) before the focal point ($Z < 0$) and a minimum transmittance (valley) after the focal point ($Z > 0$). This "peak-before-valley" characteristic curve is a typical manifestation of a negative n_2 value (self-defocusing effect).[38] In contrast, the n_2 value of $Nd{:}MoS_2$ nanosheets is 1.15×10^{-12} m^2/W, and its CA Z-scan curve (Fig. 9b) shows a transmittance minimum (valley) before the focus and a transmittance maximum (peak) after the focus. This "valley-then-peak" characteristic curve is a typical feature of a positive n_2 value (self-focusing effect). Therefore, Nd^{3+} doping changes the nonlinear refractive properties of MoS_2 nanosheets from self-defocusing (negative n_2) to self-focusing (positive n_2). Nd^{3+} doping introduces low-energy defect states into MoS_2, making the laser energy at 532 nm (2.33 eV) significantly larger than the transition energy, thereby satisfying the resonance condition. This resonant effect first greatly enhances the nonlinear absorption ($Im\chi^{(3)}$) (Table 1). According to the Kramers-Kronig relation, this change in absorption subsequently drives the nonlinear refractive behavior to switch from non-resonant self-defocusing to resonant self-focusing. This defect-engineering-mediated physical mechanism, which utilizes resonance conditions to tailor the nonlinear polarizability, provides a key pathway for customizing the nonlinear optical properties of two-dimensional materials.[39] This strategy significantly alters the material's NLR response, offering new possibilities for its application in nonlinear photonic devices, such as phase modulators based on self-focusing or self-defocusing effects.

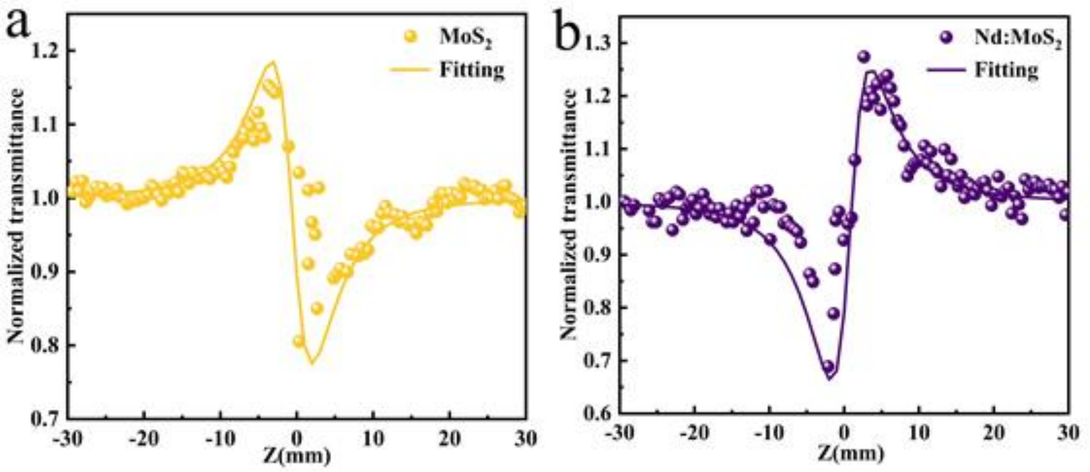

Fig. 9: CA Z-scan curves of MoS_2 (a) and $Nd{:}MoS_2$ (b) nanosheets under an excitation wavelength of 532 nm.

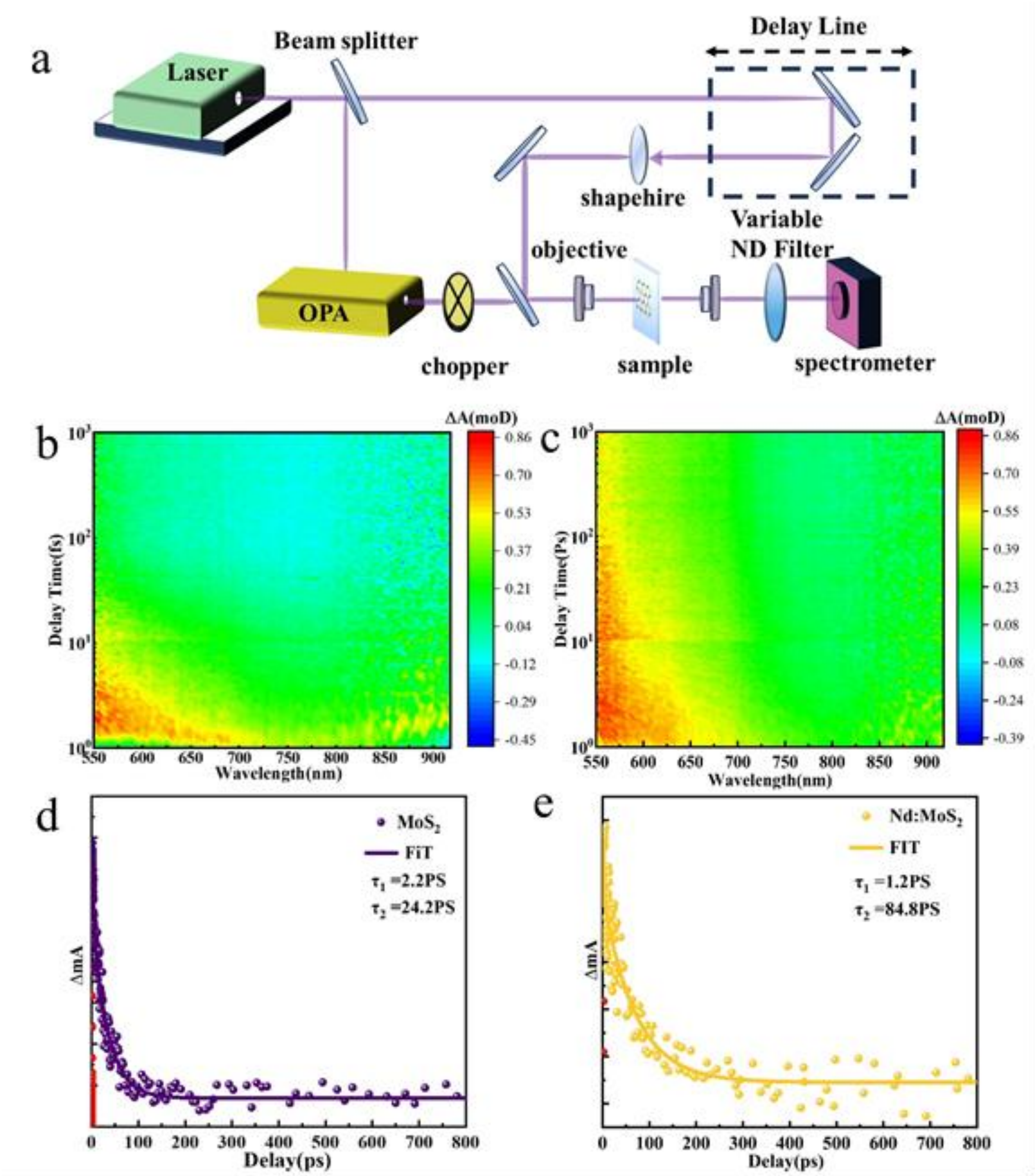

Fig. 10: (a) Schematic diagram of the micro-region femtosecond pump-probe setup. (b, c) Two-dimensional maps of pump-probe time delay for MoS_2 and $Nd{:}MoS_2$ nanosheets, respectively (probe wavelength range: approximately 525 nm to 900 nm). (d, e) Carrier decay dynamics of MoS_2 and $Nd{:}MoS_2$ nanosheets at the corresponding probe peak wavelengths, with the solid lines representing the fitting curves.

To further characterize the effect of Nd^{3+} doping on the nonlinear optical properties of $Nd{:}MoS_2$ nanosheets, femtosecond time-resolved pump-probe spectroscopy was used to measure the transient absorption spectra of the synthesized MoS_2 and $Nd{:}MoS_2$ nanosheets, in order to explore their ultrafast NLO response and carrier dynamics. The measurement schematic diagram is illustrated in Fig. 10(a). The three-dimensional TA spectra of MoS_2 and $Nd{:}MoS_2$ nanosheets obtained under excitation with a 400 nm femtosecond laser pulse were provided in Figs. 10 (b, c). A significant positive absorption signal (ΔA > 0) was observed near a wavelength of approximately 600 nm, which corresponds to ESA.[40] The ESA observed in this experiment mainly originates from the transition of photogenerated carriers within the CB or to higher energy levels. The transient absorption dynamics decay curves obtained experimentally were fitted and analyzed using a bi-exponential function, as described by Eq. (9):[41,42]

$$\Delta A(t,w) = D_1 e^{-t/\tau_1} + D_2 e^{-t/\tau_2} \qquad (9)$$

Among them, D_1 (D_2) and τ_1 (τ_2) represent the amplitude and time constant of the fast (slow) decay component, respectively. The fitting results are shown in Figs. 10(d, e). For MoS_2 nanosheets, the fast relaxation time constant $\tau_1 \approx 2.2$ ps and the slow relaxation time constant $\tau_2 \approx 24.3$ ps. For Nd:MoS_2 nanosheets, $\tau_1 \approx 1.2$ ps and $\tau_2 \approx 84.8$ ps. The fast relaxation process (τ_1) corresponds to the rapid capture of carriers by V_S defects in MoS_2 and by both Vs and Nd^{3+} trap centers in Nd:MoS_2, while the slow relaxation process (τ_2) corresponds to the recombination of photogenerated electron-hole pairs, including both radiative and non-radiative recombination. The observed reduction in τ_1 from 2.2 ps to 1.2 ps suggests that Nd^{3+} doping introduces new and efficient trap sites in Nd:MoS_2, thereby enhancing the rate of initial carrier capture. Meanwhile, τ_2 is significantly prolonged from 24.3 ps to 84.8 ps, indicating that the carriers localized at defect sites or trap states exhibit an extended lifetime. These long-lived carriers have a higher probability of being re-excited by the pump light to a higher excited state, leading to excited-state absorption (ESA).[40] Therefore, the enhanced excited-state absorption process in Nd:MoS_2 indicates that the excited-state absorption cross-section ε_2 is increased relative to the ground-state absorption cross-section ε_1, which is a key factor leading to the enhanced RSA behavior. At the same time, the dominant carrier recombination pathway may also be altered due to the presence of trap states. In summary, the TA measurement results from this study directly reveal the significant modulation effect of defect states introduced by Nd^{3+} doping on the carrier dynamics and NLA properties of Nd:MoS_2 nanosheets, providing crucial evidence for the observed changes in their NLO performance. Meanwhile, the significant PL enhancement in Nd:MoS_2 nanosheets is also validated by achieving efficient synergy between rapid carrier capture to avoid non-radiative losses and prolonged residence to promote radiative recombination.

4. Conclusion

This study demonstrates that few-layer Nd:MoS_2 nanosheets co-modified with V_S defects and Nd^{3+} doping were successfully prepared via a one-step hydrothermal method. Structural characterization confirmed that Nd^{3+} incorporation induced lattice expansion, a p-type transition, and bandgap narrowing. The synergistic effect significantly reduced the optical bandgap from 1.28 eV to 0.45 eV, extending the photoresponse into the NIR region, while also doubling the PL intensity. Nonlinear optical measurements revealed that at 532 nm, Nd:MoS_2 exhibited enhanced RSA, with the nonlinear absorption coefficient β increasing from 8.5 cm/GW to 12 cm/GW. Under 1064 nm NIR irradiation, Nd:MoS_2 for the first time demonstrated intensity-dependent controllable switching between SA and RSA. Furthermore, doping shifted the nonlinear refractive behavior from self-defocusing to self-focusing. Femtosecond transient absorption spectroscopy and theoretical calculations indicated that the synergy between Nd^{3+} energy levels and V_S defect states accelerated carrier trapping of τ_1 shortened to 1.2 ps, prolonged the non-radiative recombination lifetime of τ_2 reaching 84.8 ps, and increased excited-state absorption channels and cross-sections. This mechanism accounts for the enhanced RSA in the visible region and the excitation-state-absorption-dominated SA/RSA switching in the NIR region. The material shows promising potential for NIR photonic devices such as ultrafast lasers, optical limiters, all-optical switches, and phase modulators.

Acknowledgments

This work was supported by the National Innovation Demonstration Zones and Collaborative Innovation Platform Project for Fuzhou-Xiamen-Quanzhou (Grant No. 3502ZCQXT2023005), the Foreign Cooperation Projects (Industrialization) of Fujian Province (Grant No. 2024I1009), the Fujian Province regional development project (Grant No. 2024H4014) and the Program for Innovative Research Team in Science and Technology in Fujian Province University (IRTSTFJ).

Conflict of Interest

The authors declare that they have no conflict of interest.

Supporting Information

Applicable.

CRediT Statement

Lihua Liu: Writing - Original draft, Methodology, Conceptualization. **Zhixiang Cui:** Writing, Review & editing, Supervision, Conceptualization, Funding acquisition. **Hengyu Zhao:** Visualization, Formal analysis. **Jia Pan:** Data curation, Methodology. **Sen Zeng:** Software, Methodology, Investigation. **Qianting Wang:** Resources, Project administration. **Xiaolong Wang:** Visualization, Formal analysis, Data curation. **Junhui Si:** Conceptualization, Supervision, Project administration, Funding acquisition.

References

[1] H. Li, S. Chen, D. W. Boukhvalov, Z. Yu, M. G. Humphrey, Z. Huang, C. Zhang, Switching the nonlinear optical absorption of titanium carbide MXene by modulation of the surface terminations, *ACS Nano*, 2022, **16**, 394-404, doi: 10.1021/acsnano.1c07060.

[2] D. Pierucci, H. Henck, Z. Ben Aziza, C. H. Naylor, A. Balan, J. E. Rault, M. G. Silly, Y. J. Dappe, F. Bertran, P. Le Fèvre, F. Sirotti, A. T. Charlie Johnson, A. Ouerghi, Tunable doping in hydrogenated single layered molybdenum disulfide, *ACS Nano*, 2017, **11**, 1755-1761, doi: 10.1021/acsnano.6b07661.

[3] J. Tang, J. Huang, D. Ding, S. Zhang, X. Deng, Research progress of 1T-MoS_2 in electrocatalytic hydrogen evolution, *International Journal of Hydrogen Energy*, 2022, **47**, 39771-

39795, doi: 10.1016/j.ijhydene.2022.09.162.

[4] V. Klimas, C. Bittencourt, G. Valušis, A. Jagminas, Calcination effects of 2D molybdenum disulfides, *Materials Characterization*, 2021, **179**, 111351, doi: 10.1016/j.matchar.2021.111351.

[5] Z. Lei, X. Yu, Y. Zhang, J. Zhan, Thermally stable fishnet-like 1T-MoS_2/CNT heterostructures with improved electrode performance, *Journal of Materials Chemistry A*, 2021, **9**, 4707-4715, doi: 10.1039/d0ta10812j.

[6] K. Y. Thai, I. Park, B. J. Kim, A. T. Hoang, Y. Na, C. U. Park, Y. Chae, J.-H. Ahn, MoS_2/graphene photodetector array with strain-modulated photoresponse up to the near-infrared regime, *ACS Nano*, 2021, **15**, 12836-12846, doi: 10.1021/acsnano.1c04678.

[7] M. J. Park, K. Park, H. Ko, Near-infrared photodetector achieved by chemically-exfoliated multilayered MoS_2 flakes, *Applied Surface Science*, 2018, **448**, 64-70, doi: 10.1016/j.apsusc.2018.04.085.

[8] R. Quirós-Ovies, P. Bastante, S. Hettler, V. Vega-Mayoral, S. Aina, V. Balos, T. Pucher, A. Castellanos-Gomez, R. Arenal, J. Cabanillas-Gonzalez, E. M. Pérez, J. Santamaría, V. Sebastian, Chemically-linked heterostructures of palladium nanosheets and 2H-MoS_2, *Small*, 2024, 2406030, doi: 10.1002/smll.202406030.

[9] S.-S. Chee, W.-J. Lee, Y.-R. Jo, M. K. Cho, D. Chun, H. Baik, B.-J. Kim, M.-H. Yoon, K. Lee, M.-H. Ham, Atomic vacancy control and elemental substitution in a monolayer molybdenum disulfide for high performance optoelectronic device arrays, *Advanced Functional Materials*, 2020, **30**, 1908147, doi: 10.1002/adfm.201908147.

[10] B. Zheng, J. Fan, B. Chen, X. Qin, J. Wang, F. Wang, R. Deng, X. Liu, Rare-earth doping in nanostructured inorganic materials, *Chemical Reviews*, 2022, **122**, 5519-5603, doi: 10.1021/acs.chemrev.1c00644.

[11] H. Chen, Z. Jiang, H. Hu, B. Kang, B. Zhang, X. Mi, L. Guo, C. Zhang, J. Li, J. Lu, L. Yan, Z. Fu, Z. Zhang, H. Zheng, H. Xu, Sub-50-ns ultrafast upconversion luminescence of a rare-earth-doped nanoparticle, *Nature Photonics*, 2022, **16**, 651-657, doi: 10.1038/s41566-022-01051-6.

[12] A. Sandhyarani, M. K. Kokila, G. P. Darshan, S. C. Sharma, D. Kavyashree, H. B. Premkumar, H. Nagabhushana, Photometric features and intense blue light emanation of Nd^{3+} doped $SrTiO_3$ based nanophosphor for multi-functional applications, *Journal of Science: Advanced Materials and Devices*, 2020, **5**, 487-496, doi: 10.1016/j.jsamd.2020.08.003.

[13] B. Marappa, M. S. Rudresha, R. B. Basavaraj, G. P. Darshan, B. D. Prasad, S. C. Sharma, S. Sivakumari, P. Amudha, H. Nagabhushana, EGCG assisted Y_2O_3: Eu^{3+} nanopowders with 3D micro-architecture assemblies useful for latent finger print recognition and anti-counterfeiting applications, *Sensors and Actuators B: Chemical*, 2018, **264**, 426-439, doi: 10.1016/j.snb.2018.02.133.

[14] S. Talapatra, U. Das, M. Galib, M. J. Ferdous Anik, S. Rahman Mim, H. Saha, A. Dastider, M. S. Islam, M. A. Gafur, M. M. Billah, Enhanced opto-electronic properties of Nd doped CuO thin film, *Ceramics International*, 2024, **50**, 27699-27709, doi: 10.1016/j.ceramint.2024.05.067.

[15] Y. L. Huang, Y. Chen, W. Zhang, S. Y. Quek, C.-H. Chen, L.-J. Li, W.-T. Hsu, W.-H. Chang, Y. J. Zheng, W. Chen, A. T. S. Wee, Bandgap tunability at single-layer molybdenum disulphide grain boundaries, *Nature Communications*, 2015, **6**, 6298, doi: 10.1038/ncomms7298.

[16] C. Chong, H. Liu, S. Wang, K. Yang, First-principles study on the effect of strain on single-layer molybdenum disulfide, *Nanomaterials*, 2021, **11**, 3127, doi: 10.3390/nano11113127.

[17] P. Sundara Venkatesh, N. Kannan, M. Ganesh Babu, G. Paulraj, K. Jeganathan, Transition metal doped MoS_2 nanosheets for electrocatalytic hydrogen evolution reaction, *International Journal of Hydrogen Energy*, 2022, **47**, 37256-37263, doi: 10.1016/j.ijhydene.2022.01.109.

[18] H. Chen, X. Yang, P. Lv, P. Tian, S. Wan, Q. Liu, Mn-doped FeS with larger lattice spacing as advance anode for sodium ion half/full battery, *Chemical Engineering Journal*, 2022, **450**, 137960, doi: 10.1016/j.cej.2022.137960.

[19] T. Lv, Y. Yao, N. Li, T. Chen, Highly stretchable supercapacitors based on aligned carbon nanotube/molybdenum disulfide composites, *Angewandte Chemie International Edition*, 2016, **55**, 9191-9195, doi: 10.1002/anie.201603356.

[20] D. Ghosh, M. Ghosal Chowdhury, R. Biswas, K. K. Haldar, A. Patra, Europium molybdate/molybdenum disulfide nanostructures with efficient electrocatalytic activity for the hydrogen evolution reaction, *ACS Applied Nano Materials*, 2023, **6**, 7218-7228, doi: 10.1021/acsanm.3c00297.

[21] A. Matei, V. Ţucureanu, M. C. Popescu, C. Romaniţan, I. Mihalache, Influence of Cu dopant on the morpho-structural and optical properties ZnO nanoparticles, *Ceramics International*, 2019, **45**, 10826-10833, doi: 10.1016/j.ceramint.2019.02.158.

[22] S. Rozenfeld, H. Teller, M. Schechter, R. Farber, O. Krichevski, A. Schechter, R. Cahan, Exfoliated molybdenum di-sulfide (MoS_2) electrode for hydrogen production in microbial electrolysis cell, *Bioelectrochemistry*, 2018, **123**, 201-210, doi: 10.1016/j.bioelechem.2018.05.007.

[23] M. Li, J. Yao, X. Wu, S. Zhang, B. Xing, X. Niu, X. Yan, Y. Yu, Y. Liu, Y. Wang, P-type doping in large-area monolayer MoS_2 by chemical vapor deposition, *ACS Applied Materials & Interfaces*, 2020, **12**, 6276-6282, doi: 10.1021/acsami.9b19864.

[24] X. Huang, H. Xu, D. Cao, D. Cheng, Interface construction of P-Substituted MoS_2 as efficient and robust electrocatalyst for alkaline hydrogen evolution reaction, *Nano Energy*, 2020, **78**,

105253, doi: 10.1016/j.nanoen.2020.105253.

[25] C. Maddi, J. R. Aswin, A. Scott, Z. Aslam, E. Willneff, K. N. V. D. Adarsh, A. Jha, Structural, spectroscopic, and excitonic dynamic characterization in atomically thin Yb^{3+}-doped MoS_2, fabricated by femtosecond pulsed laser deposition, *Advanced Optical Materials*, 2019, **7**, 1900753, doi: 10.1002/adom.201900753.

[26] M. Meng, X. Ma, Improving the photoelectric characteristics of MoS_2 thin films by doping rare earth element erbium, *Nanoscale Research Letters*, 2016, **11**, 513, doi: 10.1186/s11671-016-1729-6.

[27] K. Fabrizio, K. N. Le, A. B. Andreeva, C. H. Hendon, C. K. Brozek, Determining optical band gaps of MOFs, *ACS Materials Letters*, 2022, **4**, 457-463, doi: 10.1021/acsmaterialslett.1c00836.

[28] J. Dong, L. Zhang, K. Lau, Y. Shu, S. Wang, Z. Fu, Z. Wu, X. Liu, B. Sa, J. Pei, J. Zheng, H. Zhan, Q. Wang, Tailoring broadband nonlinear optical characteristics and ultrafast photocarrier dynamics of Bi_2O_2S nanosheets by defect engineering, *Small*, 2024, **20**, 2309595, doi: 10.1002/smll.202309595.

[29] J. Li, X. Wu, W. Pan, G. Zhang, H. Chen, Vacancy-rich monolayer BiO_{2-x} as a highly efficient UV, visible, and near-infrared responsive photocatalyst, *Angewandte Chemie International Edition*, 2018, **57**, 491-495, doi: 10.1002/anie.201708709.

[30] S. Karmakar, U. Chatterjee, P. Kumbhakar, Transition from saturable absorption to reverse saturable absorption in multi-layered WS_2 nanosheets, *Optics & Laser Technology*, 2021, **136**, 106696, doi: 10.1016/j.optlastec.2020.106696.

[31] C. Quan, M. He, C. He, Y. Huang, L. Zhu, Z. Yao, X. Xu, C. Lu, X. Xu, Transition from saturable absorption to reverse saturable absorption in $MoTe_2$ nano-films with thickness and pump intensity, *Applied Surface Science*, 2018, **457**, 115-120, doi: 10.1016/j.apsusc.2018.06.245.

[32] K. Wang, Y. Feng, C. Chang, J. Zhan, C. Wang, Q. Zhao, J. N. Coleman, L. Zhang, W. J. Blau, J. Wang, Broadband ultrafast nonlinear absorption and nonlinear refraction of layered molybdenum dichalcogenide semiconductors, *Nanoscale*, 2014, **6**, 10530-10535, doi: 10.1039/c4nr02634a.

[33] P. Kurian, C. Vijayan, K. Sathiyamoorthy, C. Suchand Sandeep, R. Philip, Excitonic transitions and off-resonant optical limiting in CdS quantum dots stabilized in a synthetic glue matrix, *Nanoscale Research Letters*, 2007, **2**, 561, doi: 10.1007/s11671-007-9099-8.

[34] C. Lu, H. Xuan, Y. Zhou, X. Xu, Q. Zhao, J. Bai, Saturable and reverse saturable absorption in molybdenum disulfide dispersion and film by defect engineering, *Photonics Research*, 2020, **8**, 1512, doi: 10.1364/prj.395870.

[35] G.-F. Gao, Z.-K. Chen, K.-S. Lin, Z.-L. Li, H.-T. Gu, Y. Gao, Y. Miao, Y. Wu, X. Hu, L. Polavarapu, X.-F. Jiang, Unusual nonlinear absorption switching in mixed-halide perovskites by light-induced halide segregation, *Laser & Photonics Reviews*, 2025, **19**, 2400564, doi: 10.1002/lpor.202400564.

[36] Q. Liao, Q. Zhang, X. Wang, X. Li, G. Deng, Z. Meng, K. Xi, P. Zhan, Facile fabrication of POSS-Modified MoS_2/PMMA nanocomposites with enhanced thermal, mechanical and optical limiting properties, *Composites Science and Technology*, 2018, **165**, 388-396, doi: 10.1016/j.compscitech.2018.07.008.

[37] V. V. Vanyukov, M. V. Shuba, A. G. Nasibulin, Y. P. Svirko, P. P. Kuzhir, G. M. Mikheev, Saturable absorption and nonlinear refraction in free-standing carbon nanotube film: Theory and experiment, *Carbon*, 2022, **186**, 509-519, doi: 10.1016/j.carbon.2021.10.054.

[38] P. A. Hind, P. S. Patil, N. B. Gummagol, U. K. Goutam, B. V. Rajendra, Photoluminescence and third-order nonlinear optical limiting properties of $Sn_{1-x}Nd_xO_2$ thin films deposited *via* spray pyrolysis, *Ceramics International*, 2023, **49**, 30060-30075, doi: 10.1016/j.ceramint.2023.06.263.

[39] T. Ahmad Dar, A. Agrawal, P. K. Sen, R. J. Choudhary, P. Sen, Thermo-optic coefficients of pure and Ni doped ZnO thin films, *Thin Solid Films*, 2016, **603**, 115-118, doi: 10.1016/j.tsf.2016.01.059.

[40] X.-Y. Chen, Y. Zhao, Z.-H. Liu, Y.-T. Pang, D.-G. Wei, J.-Y. Wangchen, C.-B. Yao, Tungsten interior doping engineering induced sulfur vacancies of MoS_2 for efficient charge transfer and nonlinear optical performance: Implications for optical limiting devices, *Applied Surface Science*, 2025, **682**, 161686, doi: 10.1016/j.apsusc.2024.161686.

[41] Y. Ye, Y. Xian, J. Cai, K. Lu, Z. Liu, T. Shi, J. Du, Y. Leng, R. Wei, W. Wang, X. Liu, G. Bi, J. Qiu, Linear and nonlinear optical properties of few-layer exfoliated SnSe nanosheets, *Advanced Optical Materials*, 2019, **7**, 1800579, doi: 10.1002/adom.201800579.

[42] Y. Jiang, L. Miao, G. Jiang, Y. Chen, X. Qi, X.-F. Jiang, H. Zhang, S. Wen, Broadband and enhanced nonlinear optical response of MoS_2/graphene nanocomposites for ultrafast photonics applications, *Scientific Reports*, 2015, **5**, 16372, doi: 10.1038/srep16372.

Open Access